Schweizerischer Erdbebendienst
Service Sismologique Suisse
Servizio Sismico Svizzero
Swiss Seismological Service

ETH zürich

Triesenberg - Werkhof, FL (STRW)

SITE CHARACTERIZATION REPORT

Jan BURJÁNEK, Manuel HOBIGER, Donat FÄH

Sonneggstrasse 5 CH-8092 Zürich Switzerland; E-mail: burjanek@sed.ethz.ch

Last modified : August 28, 2015

Abstract

Ambient vibration array measurements were performed to characterize the site Triesenberg, in Liechtenstein. The site, where the new strong motion station STRW was installed, is located on the Triesenberg landslide. The new station was installed in the frame of the Renewal of strong motion seismic network in the Principality Liechtenstein project. In order to characterize the velocity profile under the station, array measurements with a $330\,\mathrm{m}$ aperture were performed. The measurements were successful and allowed deriving a velocity model for this site. We found a gradient velocity profile with the depth increasing velocity. Velocitites reach $250 - 300\,\mathrm{m/s}$ close to the surface, increase gradually to $600 - 700\,\mathrm{m/s}$ at depth $25\,\mathrm{m}$, and further increase $900 - 1500\,\mathrm{m/s}$ at depth $50\,\mathrm{m}$. The uncertainty increase gradually with the depth as well. The bedrock depth is not well constrained, but the data require maximum velocity of at least $1500\,\mathrm{m/s}$, at minimum depth of $40\,\mathrm{m}$ (or more).
$V_{s,30}$ is $449\,\mathrm{m/s}$ would generally correspond to ground type B in the Eurocode 8 [CEN, 2004], and C (according to $V_{s,30}$) for the SIA261 [SIA, 2014]. The theoretical 1D SH transfer function and impedance contrast of the quarter-wavelength velocity computed from the inverted profiles show moderate amplifications at clearly defined resonance frequencies. Recordings on the new station will allow to compare to these simple models.

Contents

1 Introduction **4**

2 Geology **5**

3 Experiment description **5**

3.1 Ambient Vibrations 5

3.2 Equipment 6

3.3 Geometry of the arrays 6

3.4 Positioning of the stations 6

4 Data quality **8**

4.1 Usable data 8

4.2 Data processing 8

5 H/V processing **9**

5.1 Processing method and parameters 9

5.2 Results 9

5.3 Polarization analysis 10

6 Array processing **13**

6.1 Processing methods and parameters 13

6.2 Obtained dispersion curves 13

7 Inversion and interpretation **16**

7.1 Inversion 16

7.2 Travel time average velocities and ground type 18

7.3 SH transfer function and quarter-wavelength velocity 18

8 Conclusions **20**

References **23**

1 Introduction

The station STRW (Triesenberg - Werkhof, FL) is part of the strong motion network of the Principality Liechtenstein, and is run within the Swiss Strong Motion Network (SSMNet). STRW has been installed in the framework of the Renewal of strong motion seismic network in the Principality Lichtenstein project in 2014. This project includes also the site characterization. Passive array measurements have been selected as a standard tool to investigate these sites. An array measurement was carried out on 20th November 2014 in the rural area, close to the road maintenance depot of the Triesenberg municipality (Fig. 1). The array consisted of four eccentric rings (polygons). A vertex of the smallest ring was close to STRW, whereas STRW is located rather at the central part of the outer rings. Such irregular configuration was selected in order to characterize the velocity profile under the STRW station and reducing the influence of local sources due to the road maintenance depot which is close by. This report presents the measurement setup, the results of the H/V analysis and of the array processing of the surface waves (dispersion curves). Then, an inversion of these results into velocity profiles is performed. Standard parameters are derived to evaluate the amplification at this site.

Staat	City	Location	Station code	Site type	Slope
Liechtenstein	Triesenberg	Werkhof	STRW	Active landslide	Slope

Table 1: Main characteristics of the study-site.

Figure 1: Picture of the site.

2 Geology

The geological map indicates that the site is located on postglacial landslide mass. The bedrock (Fig. 2) consits of the Vorarlberger Flysch unit and contains Schists, limestones, sandstones, flysch. A more detailed geological description is provided by [Francois et al., 2007]. The station is located at the currently rather inactive deep seated landslide (depth downto $80\,\mathrm{m}$), close to the border with shallow active part ($10 - 20\,\mathrm{m}$ depth range). The active slide has an area of $3.1\,\mathrm{km}^2$ and a volume of $37\,10^6\,\mathrm{m}^3$ [Francois et al., 2007]. It consits of elements of limestone, sandstone, dolomite, flysch, and Quaternary deposits in a clayey silt matrix [Francois et al., 2007]. Considering the entire landslide, velocities of the movement range between $0 - 3\,\mathrm{cm/year}$ depending on the exact location, based on the measurements between 1976-1981 and 1996-1997 [Francois et al., 2007]. The STRW should move approximately one centimeter per year.

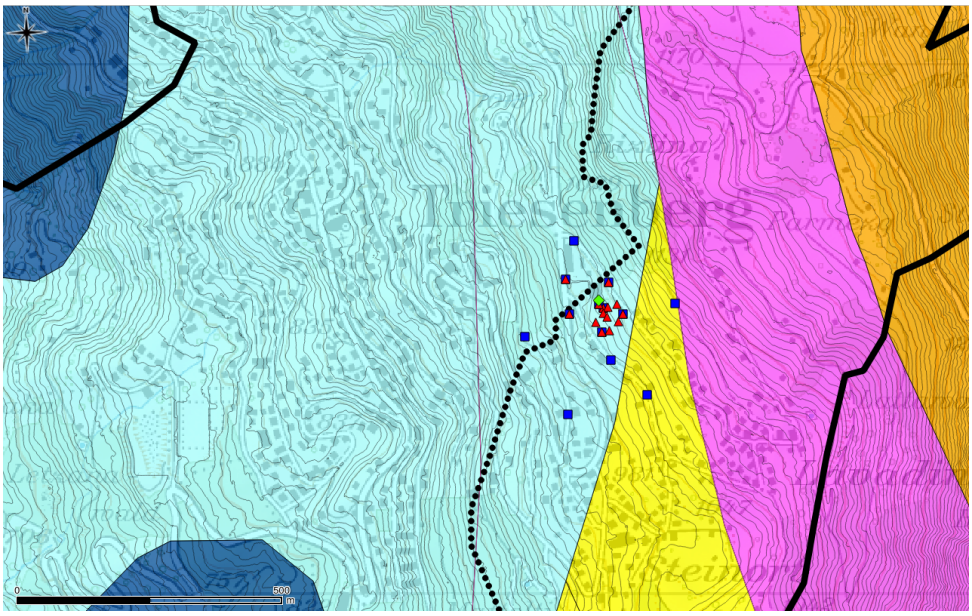

Figure 2: Geological map of the area of station STRW (green diamond) including the array (blue and red symbols). The cyan color referes to postglacial landslide mass, the dark blue to the Vorarlberger Flysch, the magenta and gold colors to the Austroalpine zone, yellow color to the Arosa zone. The black solid line shows the limits of the entire landslide, whereas the dotted line shows the border between the active shallow (to the west) and rather inactive deep seated (to the east) landslides.

3 Experiment description

3.1 Ambient Vibrations

The ground surface is permanently subjected to ambient vibrations due to:

- natural sources (ocean and large-scale atmospheric phenomena) below $1\,\mathrm{Hz}$,
- local meteorological conditions (wind and rain) at frequencies around $1\,\mathrm{Hz}$,

- human activities (industrial machines, traffic...) at frequencies above $1\,\mathrm{Hz}$ [Bonnefoy-Claudet et al., 2006].

The objective of the measurements is to record these ambient vibrations and to use their propagation properties to infer the underground structure. First, the polarization of the recorded waves (H/V ratio) is used to derive the resonance frequencies of the soil column. Second, the arrival time delays at many different stations are used to derive the velocity of surface waves at different frequencies (dispersion). The information (H/V, dispersion curves) is then used to derive the properties of the soil column using an inversion process.

3.2 Equipment

For these measurements 12 Quanterra Q330 dataloggers named NR01 to NR12 and 14 Lennartz 3C 5 s seismometers were available (see Tab. 2). Each datalogger can record on 2 ports A (channels EH1, EH2, EH3 for Z, N, E directions) and B (channels EH4, EH5, EH6 for Z, N, E directions). Time synchronization was ensured by GPS. The sensors were placed on a metal tripod, in a $20\,\mathrm{cm}$ deep hole, when necessary, for better coupling with the ground.

Digitizer	**Model**	**Number**	**Resolution**
	Quanterra Q330	12	$24\,\mathrm{bits}$
Sensor type	**Model**	**Number**	**Cut-off frequency**
Velocimeter	Lennartz 3C	14	$0.2\,\mathrm{Hz}$

Table 2: Equipment used.

3.3 Geometry of the arrays

Two array configurations were used. In the first configuration, 3 eccentric rings of approximately 10, 25 and $60\,\mathrm{m}$ radius were deployed for a total of 14 sensors. The STRW station is close to the center of the smallest ring. The configuration is quite irregular because of many obstacles (houses, streets). The second configuration includes an outer ring of approximately $160\,\mathrm{m}$ (plus the most outer ring of the first configuration and one station of the innermost ring), 13 sensors in total. The minimum inter-station distance and the aperture are therefore 10 and $120\,\mathrm{m}$ and 10 and $320\,\mathrm{m}$, respectively. The experimental setup is displayed in Fig. 3. The final usable datasets are detailed in section 4.2.

3.4 Positioning of the stations

The sensor coordinates were measured using a differential GPS device (Leica Viva GS10), including only a rover station and using the Real Time Kinematic technique provided by Swisstopo. It allows an absolute positioning with an accuracy better than $6\,\mathrm{cm}$ on the Swissgrid. This accuracy was reached for all stations.

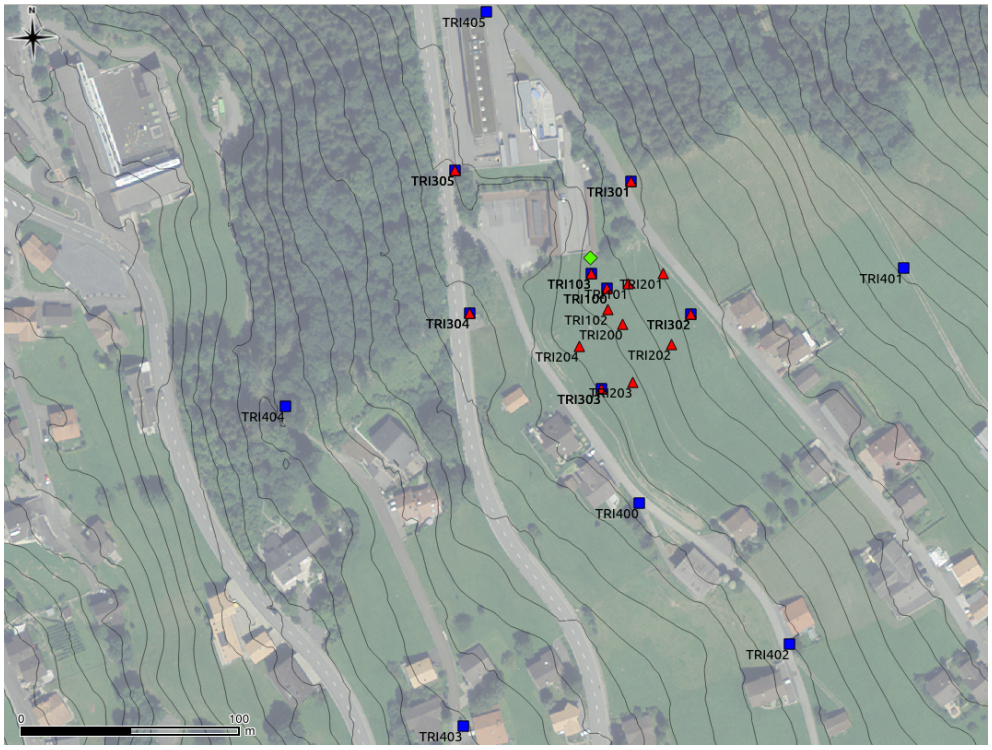

Figure 3: Geometry of the arrays. Red triangles refer to the first configuration, blue squares refer to the second configuration, and green diamond to the STRW station.

4 Data quality

4.1 Usable data

The largest time windows were extracted, for which all the sensors of the array were correctly placed and the GPS synchronization was ensured. Recordings are generally consistent. Incoherent high amplitude signals present at TRI304, TRI305, TRI405 are mainly due to car traffic, since these stations were located close to a relatively busy road. The characteristics of the datasets are detailed in Tab. 3.

4.2 Data processing

The data were first converted to SAC format including in the header the coordinates of the point (CH1903 system), the recording component and a name related to the position. The name is made of 3 letters characterizing the location (TRI here), 1 digit for the ring and 2 more digits for the number in the ring (zero for the central station of the corresponding ring - if present). Recordings were not corrected for the instrumental response.

Dataset	**Starting Date**	**Time**	**Length**	F_s	**Min. inter-distance**	**Aperture**	**# of points**
1	2014/11/20	10:45	103 min	200 Hz	10 m	120 m	14
2	2014/11/20	13:45	90 min	200 Hz	10 m	400 m	13

Table 3: Usable datasets.

5 H/V processing

5.1 Processing method and parameters

In order to process the H/V spectral ratios, several codes and methods were used. The classical H/V method was applied using the Geopsy `http://www.geopsy.org` software. In this method, the ratio of the smoothed Fourier Transform of selected time windows are averaged. Tukey windows (cosine taper of 5% width) of $50\,\mathrm{s}$ long overlapping by 50% were selected. Konno and Ohmachi [1998] smoothing procedure was used with a b value of 60. The multitaper method of the spectra estimates [Prieto et al., 2009] was applied as well with the time bandwidth product of 2.5 and 4 tapers. The classical method of Fäh et al. [2001] was also performed.

Moreover, the time-frequency analysis method [Fäh et al., 2009] was used to estimate the ellipticity function more accurately using the Matlab code of V. Poggi. In this method, the time-frequency analysis using the Wavelet transform is computed for each component. For each frequency, the maxima over time (10 per minute with at least $0.1\,\mathrm{s}$ between each) in the TFA are determined. The Horizontal to Vertical ratio of amplitudes for each maximum is then computed and statistical properties for each frequency are derived. A Cosine wavelet with parameter 9 is used. The mean of the distribution for each frequency is stored. For the sake of comparison, the time-frequency analysis of Fäh et al. [2001], based on the spectrogram, was also used.

The ellipticity extraction using the Capon analysis [Poggi and Fäh, 2010] (see section on array analysis) was also performed.

Method	Freq. band	Win. length	Anti-trig.	Overlap	Smoothing
Standard H/V Geopsy	$0.2-20\,\mathrm{Hz}$	$50\,\mathrm{s}$	No	50%	K&O 60
Standard H/V Multitaper	$0.2-40\,\mathrm{Hz}$	$200\,\mathrm{s}$	No	-	-
Standard H/V D. Fäh	$0.2-20\,\mathrm{Hz}$	$30\,\mathrm{s}$	No	75%	-
H/V TFA D. Fäh	$0.2-20\,\mathrm{Hz}$	Specgram	No	-	-
H/V TFA V. Poggi	$0.2-20\,\mathrm{Hz}$	Cosine wpar=9	No	-	No

Table 4: Methods and parameters used for the H/V processing.

5.2 Results

All the methods to compute H/V ratios are compared at station TRI103, closest to STRW (Fig. 4), in which the classical methods were divided by $\sqrt{2}$ to correct from the Love wave contribution [Fäh et al., 2001]. Overall, the classical and TFA methods match well.

All points of the array show similar same shape in their H/V with a peak (Fig. 5) at $1.6\,\mathrm{Hz}$. The potential right flank of the ellipticity curve is consistently observed between $1.6-3\,\mathrm{Hz}$. A secondary H/V peak might be idetnified between $3-5\,\mathrm{Hz}$ with variable amplitude. The H/V curves for stations of the two innermost rings are shown in Fig. 6 together with the ellipticity curves of the fundamental mode obtained by the array method. The resolution limits of the array do no allow to retrieve fundamental peaks and right flank by the array method. The high frequency part of the ellipticity curve retrieved by the array method does not show the secondary

peak and is at rather lower level with respect to single station H/V curves. Concluding, the fundamental peak at the STRW station is at $1.6\,\mathrm{Hz}$, with a peak amplitude around 3 for the TFA methods.

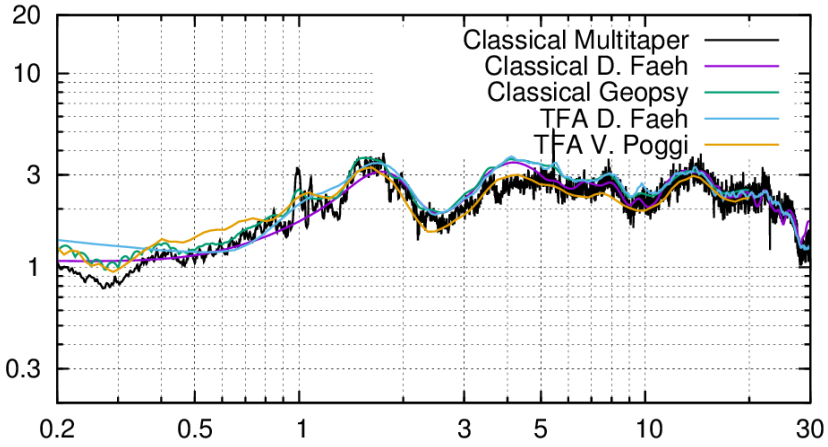

Figure 4: H/V spectral ratios for point TRI103 using the different codes. Classical methods were divided by $\sqrt{2}$.

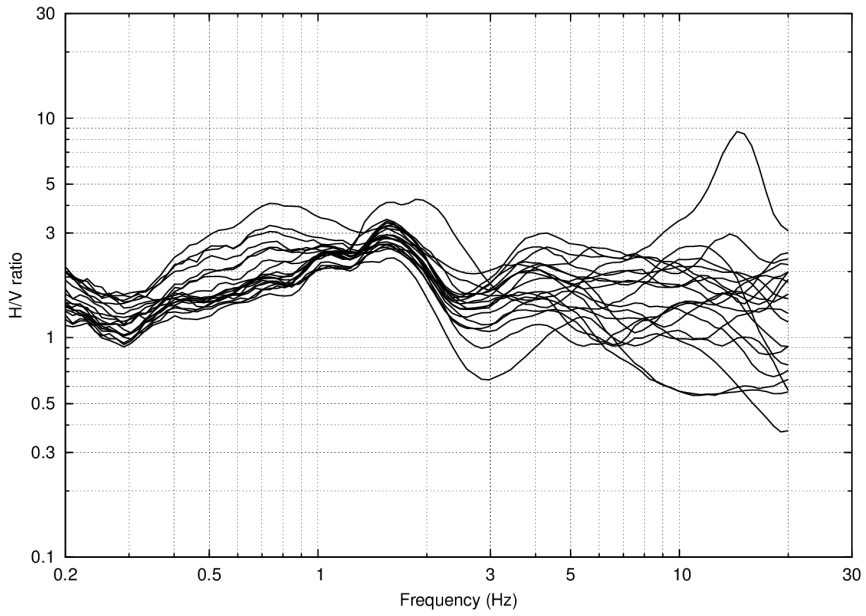

Figure 5: H/V spectral ratios (time-frequency analysis code V. Poggi).

5.3 Polarization analysis

Polarization analysis on the array data was performed using the method of Burjánek et al. [2010]. Most of the points (Fig. 7) show a weak particular East-West polarization especially in the frequency band $3-5\,\mathrm{Hz}$, which corresponds to the secondary H/V peak. Clusters of points with similar polarization can be identified. For example, stations of the outermost ring (except TRI401) and stations TRI304, TRI305 do not show the specific East-West polarization between

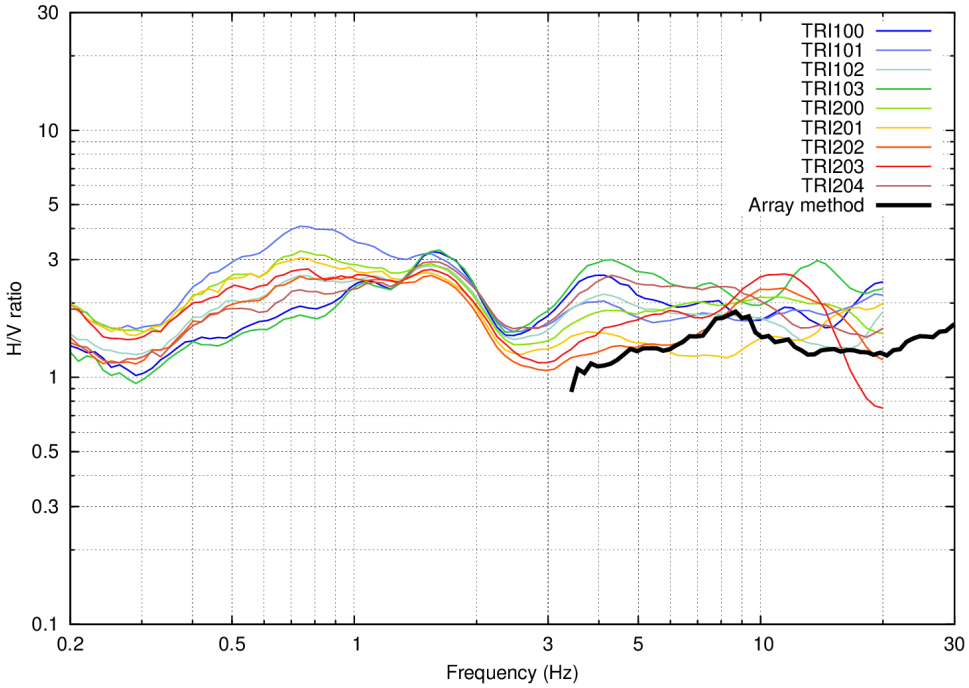

Figure 6: H/V spectral ratios for the two innermost rings. Ellipticity curves obtained by the array method are show in black.

$3 - 5\,\mathrm{Hz}$. Thus it seems, that this feature is related to the inner part of the array. However, we do not have any specific interpretation at the moment.

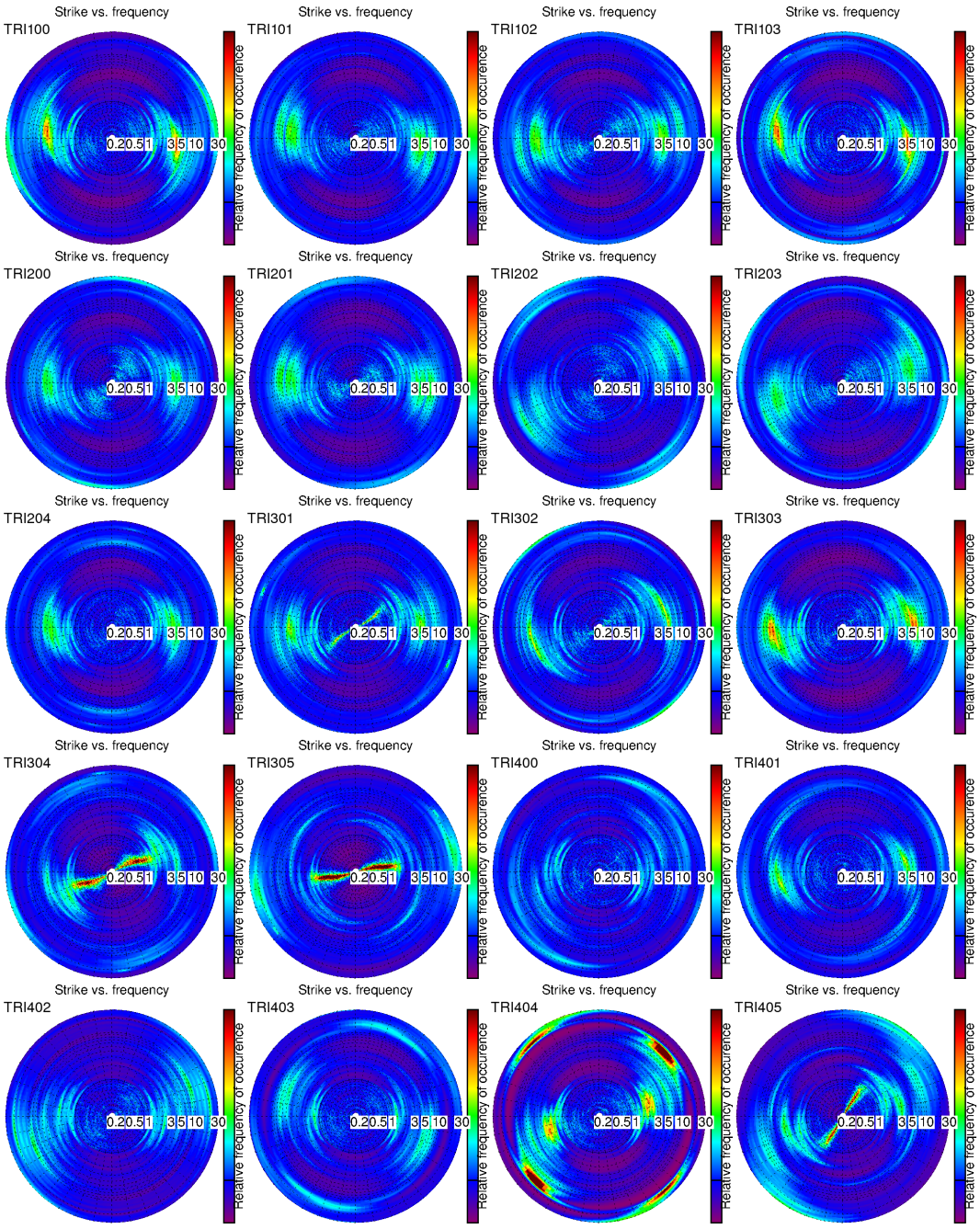

Figure 7: Strike of the polarization for all stations.

6 Array processing

6.1 Processing methods and parameters

The vertical components of the arrays were processed using the High-resolution FK (HRFK) analysis [Capon, 1969] using the Geopsy `http://www.geopsy.org` software. Better results were obtained using large time windows (200T). Moreover, a 3C array analysis [Fäh et al., 2008] was also performed using both the array_tool_3C software [Poggi and Fäh, 2010] (HRFK). It allows to derive Rayleigh and Love modes including the Rayleigh ellipticity. Since the array was deployed on a slope, the NEZ Cartesian system (North-South; East-West; Vertical) used usually in the analysis might not be the best in this case. Surface waves might rather propagate along the tilted free surface. That's why we tried to rotate both station coordinates and recording components into a new system, which has a horizontal plane parallel to the slope. In particular, we find a best fitting plane in 3D given the station coordinates (including station elevation). This best fitting plane has a strike of $152\,deg.$ and a dip (slope) of $17.5\,deg.$. We defined a new coordinate system fixed to this plane (first axis along the strike, second axis along the dip, and third axis normal to that plane). Afterwards, both recording components and station coordinates were expressed (rotated in 3D) in this new coordinate system. Finally, all array proccessing was performed with this rotated dataset as well.

Method	Set	Freq. band	Win. length	Anti-trig.	Overlap	Grid step	Grid size	# max.
HRFK 1C	1	$1-20\,\mathrm{Hz}$	$200T$	No	50%	0.0035	0.769	2
HRFK 1C	2	$1-20\,\mathrm{Hz}$	$200T$	No	50%	0.0012	0.289	2
HRFK 3C	1	$1-40\,\mathrm{Hz}$	Wav. 10	No	50%	200	2500	5
			Tap. 0.1			m/s	m/s	
HRFK 3C	2	$1-40\,\mathrm{Hz}$	Wav. 10	No	50%	200	2500	5
			Tap. 0.1			m/s	m/s	

Table 5: Methods and parameters used for the array processing (both rotated & unrotated).

6.2 Obtained dispersion curves

Selected results of the different FK analysis are presented in Fig. 8 for the vertical and in Fig. 9 for the transversal component, comparing the results for the rotated and original datasets. The rotation did not lead to better results (i.e., to a lower scatter). Just in opposite, it was possible to pick the Rayleigh fundamental mode just up to $15\,\mathrm{Hz}$ with the rotated dataset, and up to $20\,\mathrm{Hz}$ with the original dataset. All the different picks with different codes are summarized in Fig. 10. In general, the pickings are in good agreement (comparing different methods). The picking of the Love fundamental mode is the same for both rotated and original datasets. The picking of the Raleigh fundamental mode is slightly different in frequency band of 4 - $8\,\mathrm{Hz}$ for the rotated and unrotated datasets. Finally, we prefered the results for the original dataset, as it is less scattered. Rayleigh fundamental mode could be picked between 2.5 - $20\,\mathrm{Hz}$, and Love mode between 2.7 - $8.9\,\mathrm{Hz}$. All picked curves, trimmed according to the resolution limits, are presented together on Fig. 11. The potential Love 1st higher mode was not used in the inversion because of very high scatter.

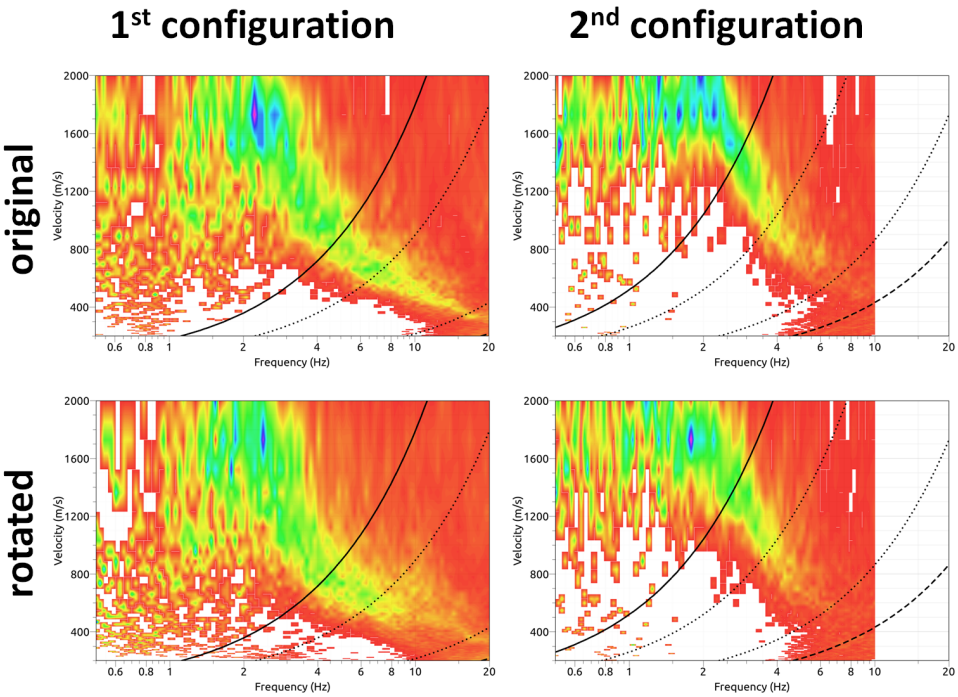

Figure 8: Dispersion curves from the 1C analysis of the vertical component. Top: Original dataset (first and second configuration); Bottom: Rotated dataset (first and second configuration).

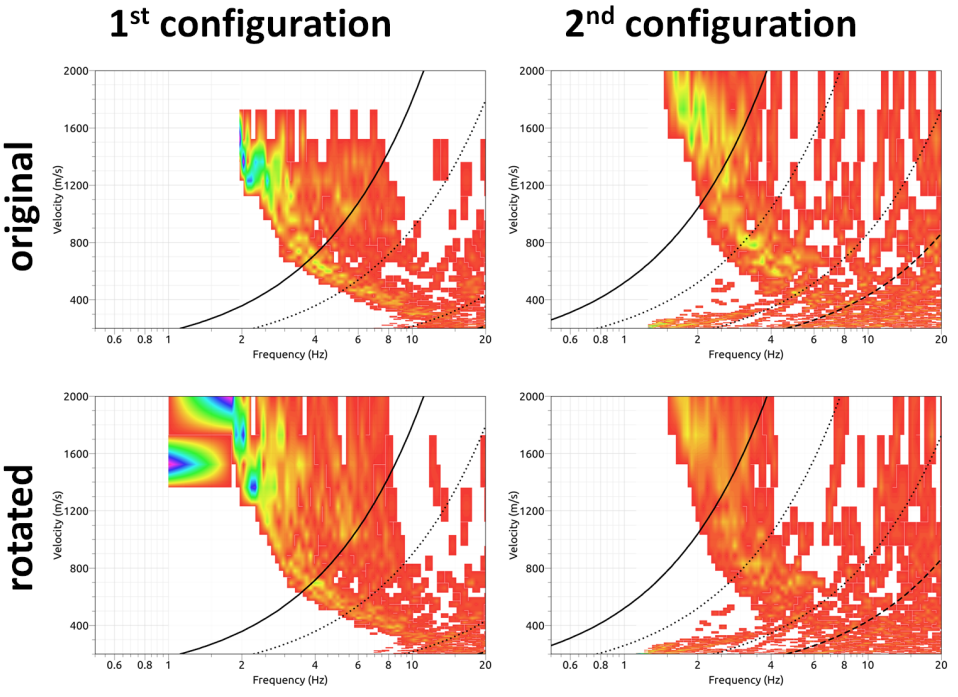

Figure 9: Dispersion curves from the 3C analysis of the transversal component. Top: Original dataset (first and second configuration); Bottom: Rotated dataset (first and second configuration).

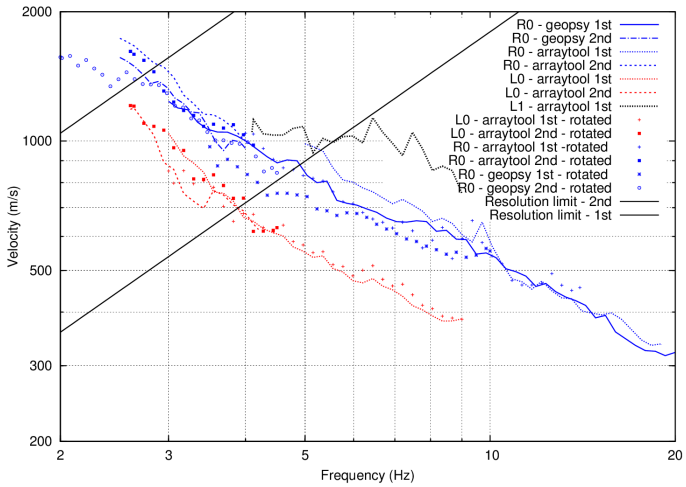

Figure 10: Picked dispersion curves from 1C and 3C HRFK methods. Colors distinguish vertical (blue) and transversal components (red). Lines show the results for the original dataset, whereas the symbols show results for the rotated datasets. The different line-styles and symbols distinguish the different methods.

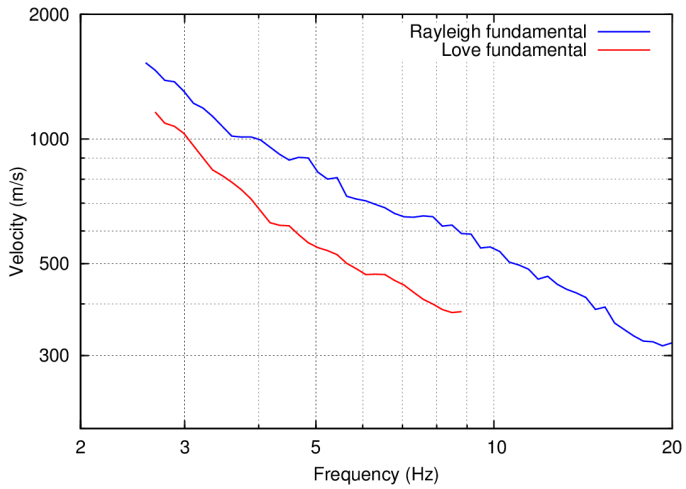

Figure 11: Final dispersion curves from 1C and 3C HRFK methods used in the inversion.

7 Inversion and interpretation

7.1 Inversion

For the inversion, Rayleigh fundamental and Love fundamental mode dispersion curves between 2.5 and $20\,\mathrm{Hz}$, as well as the ellipticity of the fundamental mode were used as simultaneous targets without standard deviation to avoid different weighting. The first higher Love mode was not used in the inversion as it was subjected to a very high uncertainty and did not seem compatible with rest of the dataset (after the first round of inversions). A very low weight of 0.01 was assigned to the ellipticity curve. All curves were resampled using 100 points between 0.5 and $20\,\mathrm{Hz}$ in log scale.

The inversion was performed using the Improved Neighborhood Algorithm (NA) Wathelet [2008] implemented in the Dinver software. In this algorithm, the tuning parameters are the following: Ns_0 is the number of starting models, randomly distributed in the parameter space, Nr is the the number of best cells considered around these Ns_0 models, Ns is the number of new cells generated in the neighborhood of the Nr cells (Ns/Nr per cell) and It_{max} is the number of iteration of this process. The process ends with $Ns_0 + Nr * \frac{Ns}{Nr} * It_{max}$ models. The used parameters are detailed in Tab. 6.

It_{max}	Ns_0	Ns	Nr
200	10000	400	100

Table 6: Tuning parameters of Neighborhood Algorithm.

The velocity was assumed to increase with depth. The Poisson ratio was inverted in each layer in the range 0.2-0.45. The density was assumed between 2100 and $2600\,\mathrm{kg/m^3}$. A number of inversions with fixed and free layer depths were performed (testing different parametrizations). Two different parametrization schemes were finally considered (20 fixed depth layers and 3 free depth layers). The three layer model (two layers over half-space) represents an extreme case, which is still capable to represent well the dispersion curves, and fits the secondary ellipticity peak. For further elaborations, the best models of these 2 runs were selected (Fig. 14) and additional 20 models for each of the two runs, which sample roughly the uncertainty of the inversion.

We found a gradient velocity profile with the depth increasing velocity. Velocitites reach $250 - 300\,\mathrm{m/s}$ close to the surface, increase gradually to $600 - 700\,\mathrm{m/s}$ at depth of $25\,\mathrm{m}$, and further increase $900 - 1500\,\mathrm{m/s}$ at depth of $50\,\mathrm{m}$. The uncertainty increase gradually with the depth as well. The bedrock depth is not well constrained, but the data require maximum velocity of at least $1500\,\mathrm{m/s}$, at minimum depth of $40\,\mathrm{m}$ (or more).

The dispersion curves are well represented. The fundamental peak of the ellipticity curve can be fitted only with the gradient model (i.e., with the fine fixed depth layering). Any stronger interface would result in a pronounced peak in the ellipticity, which is not observed.

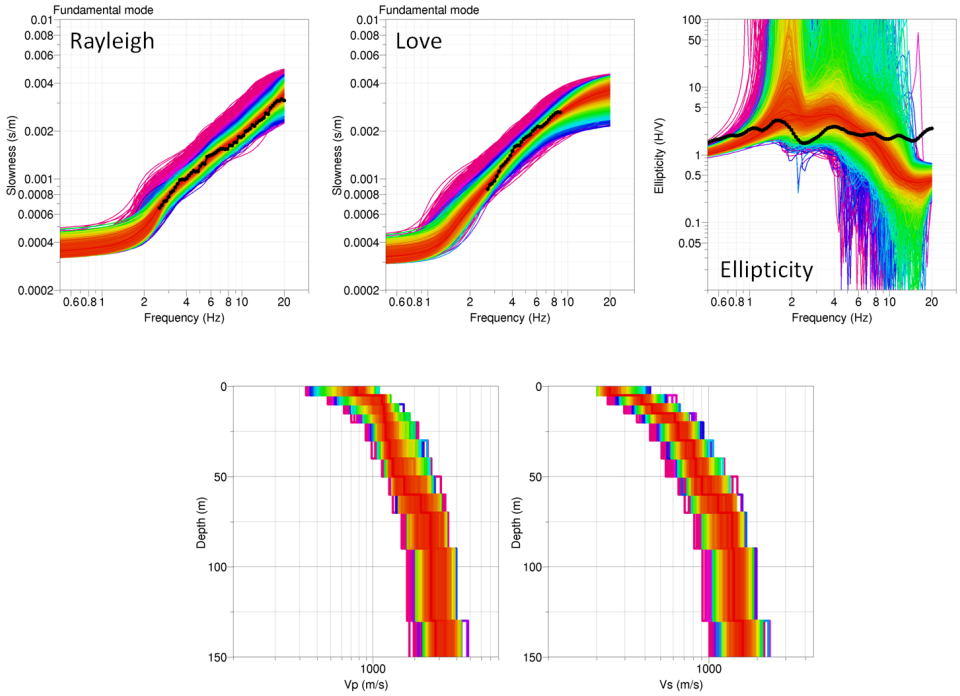

Figure 12: Comparison between inverted and measured Rayleigh, Love modes, ellipticity curves in case of fixed depth layer approach. Corresponding inverted ground profiles in terms of V_p and V_s are plotted in bottom.

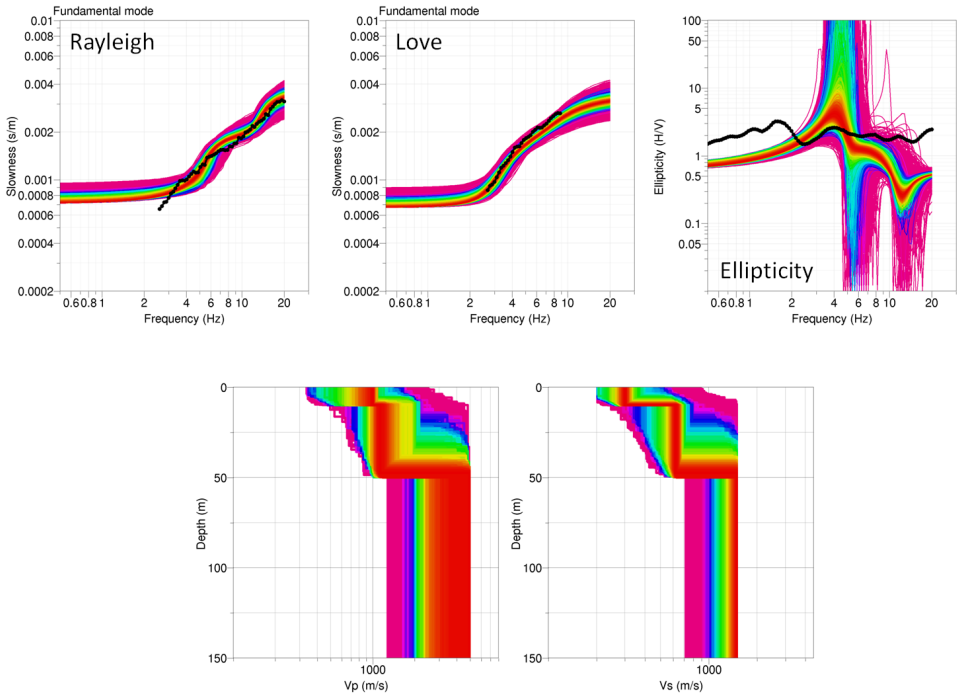

Figure 13: Comparison between inverted and measured Rayleigh, Love modes, ellipticity curves in case of free depth layer approach. Corresponding inverted ground profiles in terms of V_p and V_s are plotted in bottom.

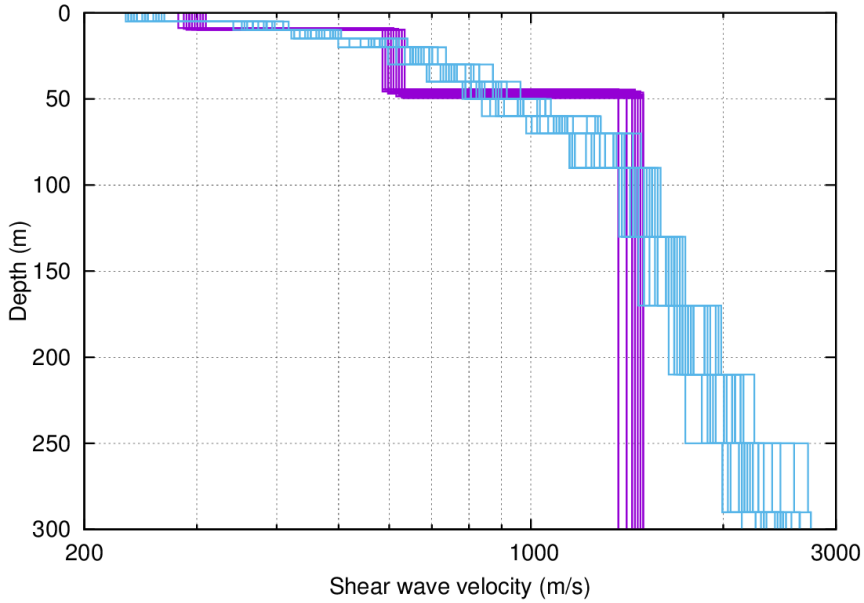

Figure 14: V_s ground profiles for the selected 40 best models. Different colors distinguish different parametrizations.

7.2 Travel time average velocities and ground type

The distribution of the travel time average velocities at different depths was computed from the selected models. The uncertainty, computed as the standard deviation of the distribution of travel time average velocities for the considered models, is also provided, but it is not guaranteed that the full range of uncertainties is covered. $V_{s,30}$ is found to be $449\,\mathrm{m/s}$, which corresponds to ground type B in the Eurocode 8 [CEN, 2004], and C for the SIA261 [SIA, 2014].

	Mean (m/s)	**Uncertainty (m/s)**
$V_{s,5}$	272	27
$V_{s,10}$	300	7
$V_{s,20}$	391	15
$V_{s,30}$	449	10
$V_{s,40}$	491	7
$V_{s,50}$	531	9
$V_{s,100}$	758	18

Table 7: Travel time averages at different depths from the inverted models. Uncertainty is given as one standard deviation from the selected profiles.

7.3 SH transfer function and quarter-wavelength velocity

The quarter-wavelength velocity approach [Joyner et al., 1981] provides, for a given frequency, the average velocity at a depth corresponding to 1/4 of the wavelength of interest. It is useful

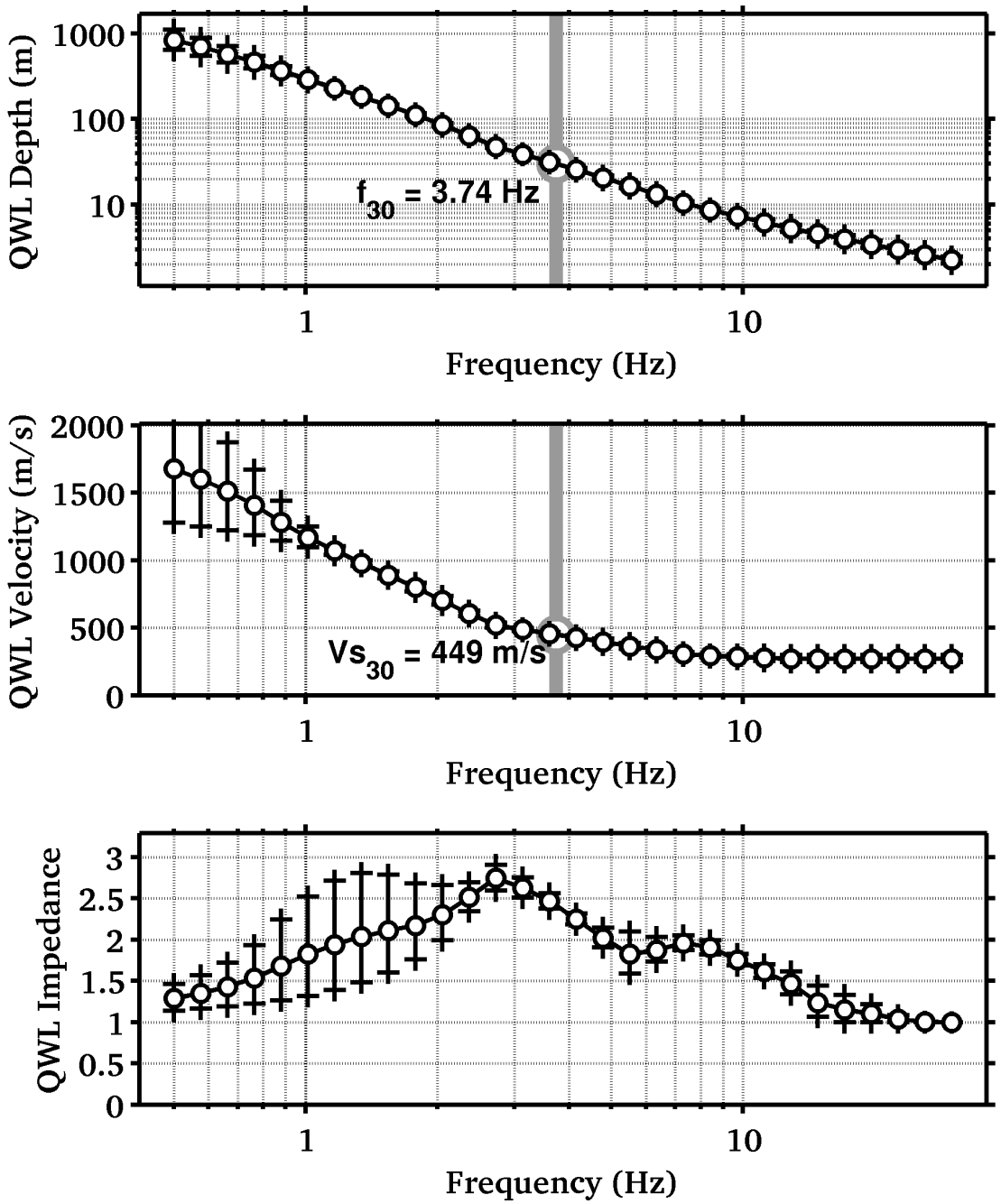

Figure 15: Quarter wavelength velocity representation of the velocity profile (top: depth, centre: velocity, bottom: inverse of the impedance contrast). Grey bar corresponds to $V_{s,30}$.

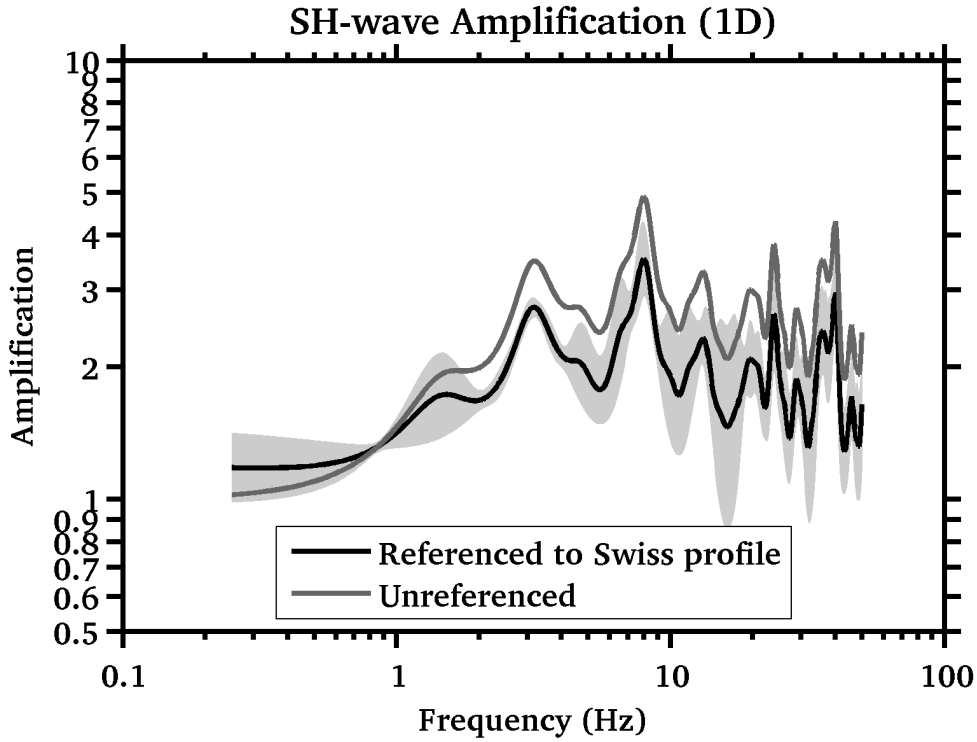

Figure 16: Theoretical SH transfer function (solid line) and quarter wavelength impedance contrast (dashed line) with their standard deviation. Significance of the greyshades is detailed in Fig. 15.

to identify the frequency limits of the experimental data (minimum frequency in dispersion curves at $2.5\,\mathrm{Hz}$ and ellipticity peak at $1.6\,\mathrm{Hz}$ here). The results using this proxy show that the dispersion curves constrain the profiles down to $50\,\mathrm{m}$ and the ellipticity down to $150\,\mathrm{m}$ (Fig. 15). Moreover, the quarter wavelength impedance-contrast introduced by Poggi et al. [2012] is also displayed in the figure. It corresponds to the ratio between two quarter-wavelength average velocities, respectively from the top and the bottom part of the velocity profile, at a given frequency [Poggi et al., 2012]. It shows a trough (inverse shows a peak) at the resonance frequency.
Moreover, the theoretical SH-wave transfer function for vertical propagation [Roesset, 1970] is computed from the inverted profiles. It is compared to the quarter-wavelength amplification [Joyner et al., 1981] that however cannot take resonances into account (Fig. 16). In this case, the models are predicting a peaky amplification up to a factor of 3 at several resonance peaks between 1 and $10\,\mathrm{Hz}$.

8 Conclusions

The array measurements presented in this study were successful in deriving a velocity model for the site of the STRW station. We found a gradient velocity profile with the depth increasing velocity. Velocitites reach $250 - 300\,\mathrm{m/s}$ close to the surface, increase gradually to $600 - 700\,\mathrm{m/s}$ at depth $25\,\mathrm{m}$, and further increase $900 - 1500\,\mathrm{m/s}$ at depth $50\,\mathrm{m}$. The uncertainty increase gradually with the depth as well. The bedrock depth is not well constrained, but the

data require maximum velocity of at least $1500\,\mathrm{m/s}$, at minimum depth of $40\,\mathrm{m}$ (or more). $V_{s,30}$ is $449\,\mathrm{m/s}$ would generally correspond to ground type B in the Eurocode 8 [CEN, 2004], and C for the SIA261 [SIA, 2014]. The theoretical 1D SH transfer function and impedance contrast of the quarter-wavelength velocity computed from the inverted profiles show significant amplifications at clearly defined resonance frequencies. Recordings on the new station will allow to compare to these simple models.

Acknowledgements

The authors thank Ulrike Kleinbrod and Felicitas Stein who helped with the measurement.

References

Sylvette Bonnefoy-Claudet, Fabrice Cotton, and Pierre-Yves Bard. The nature of noise wavefield and its applications for site effects studies. *Earth-Science Reviews*, 79(3-4): 205–227, December 2006. ISSN 00128252. doi: 10.1016/j.earscirev.2006.07.004. URL http://linkinghub.elsevier.com/retrieve/pii/S0012825206001012.

Jan Burjánek, Gabriela Gassner-Stamm, Valerio Poggi, Jeffrey R. Moore, and Donat Fäh. Ambient vibration analysis of an unstable mountain slope. *Geophysical Journal International*, 180(2):820–828, February 2010. ISSN 0956540X. doi: 10.1111/j.1365-246X.2009.04451.x. URL http://gji.oxfordjournals.org/cgi/doi/10.1111/j.1365-246X.2009.04451.xhttp://doi.wiley.com/10.1111/j.1365-246X.2009.04451.x.

J. Capon. High-Resolution Frequency-Wavenumber Spectrum Analysis. *Proceedings of the IEEE*, 57(8):1408–1418, 1969. ISSN 0018-9219. doi: 10.1109/PROC.1969.7278. URL http://ieeexplore.ieee.org/lpdocs/epic03/wrapper.htm?arnumber=1449208.

CEN. *Eurocode 8: Design of structures for earthquake resistance - Part 1: General rules, seismic actions and rules for buildings*. European Committee for Standardization, en 1998-1: edition, 2004.

Donat Fäh, Fortunat Kind, and Domenico Giardini. A theoretical investigation of average H/V ratios. *Geophysical Journal International*, 145(2):535–549, May 2001. ISSN 0956540X. doi: 10.1046/j.0956-540x.2001.01406.x. URL http://doi.wiley.com/10.1046/j.0956-540x.2001.01406.x.

Donat Fäh, Gabriela Stamm, and Hans-Balder Havenith. Analysis of three-component ambient vibration array measurements. *Geophysical Journal International*, 172(1):199–213, January 2008. ISSN 0956540X. doi: 10.1111/j.1365-246X.2007.03625.x. URL http://doi.wiley.com/10.1111/j.1365-246X.2007.03625.xhttp://gji.oxfordjournals.org/cgi/doi/10.1111/j.1365-246X.2007.03625.x.

Donat Fäh, Marc Wathelet, Miriam Kristekova, Hans-Balder Havenith, Brigitte Endrun, Gabriela Stamm, Valerio Poggi, Jan Burjánek, and Cécile Cornou. Using Ellipticity Information for Site Characterisation. Technical report, NERIES JRA4 Task B2, 2009.

B. Francois, L. Tacher, Ch. Bonnard, L. Laloui, and V. Triguero. Numerical modelling of the hydrogeological and geomechanical behaviour of a large slope movement: the Triesenberg landslide (Liechtenstein). *Canadian Geotechnical Journal*, 4(44):840–857, 2007.

William B. Joyner, Richard E. Warrick, and Thomas E. Fumal. The effect of Quaternary alluvium on strong ground motion in the Coyote Lake, California, earthquake of 1979. *Bulletin of the Seismological Society of America*, 71(4):1333–1349, 1981.

Katsuaki Konno and Tatsuo Ohmachi. Ground-Motion Characteristics Estimated from Spectral Ratio between Horizontal and Vertical Components of Microtremor. *Bulletin of the Seismological Society of America*, 88(1):228–241, 1998.

Valerio Poggi and Donat Fäh. Estimating Rayleigh wave particle motion from three-component array analysis of ambient vibrations. *Geophysical Journal International*, 180(1):251–267, January 2010. ISSN 0956540X. doi: 10.1111/j.1365-246X.2009.04402.x. URL http://doi.wiley.com/10.1111/j.1365-246X.2009.04402.x.

Valerio Poggi, Benjamin Edwards, and Donat Fäh. Characterizing the Vertical-to-Horizontal Ratio of Ground Motion at Soft-Sediment Sites. *Bulletin of the Seismological Society of America*, 102(6):2741–2756, December 2012. ISSN 0037-1106. doi: 10.1785/0120120039. URL http://www.bssaonline.org/cgi/doi/10.1785/0120120039.

G.A. Prieto, R.L. Parker, and F.L. Vernon III. A fortran 90 library for multitaper spectrum analysis. *Computers & Geosciences*, 35(8):1701 – 1710, 2009. ISSN 0098-3004. doi: http://dx.doi.org/10.1016/j.cageo.2008.06.007. URL http://www.sciencedirect.com/science/article/pii/S0098300409000077.

J.M. Roesset. Fundamentals of soil amplification. In R. J. Hansen, editor, *Seismic Design for Nuclear Power Plants*, pages 183–244. M.I.T. Press, Cambridge, Mass., 1970. ISBN 978-0-262-08041-5. URL http://mitpress.mit.edu/catalog/item/default.asp?ttype=2&tid=5998.

SIA. *SIA 261 Einwirkungen auf Tragwerke*. Schweizerischen Ingenieur- und Architektenverein, Zürich, sia 261:2014 edition, 2014.

Marc Wathelet. An improved neighborhood algorithm: Parameter conditions and dynamic scaling. *Geophysical Research Letters*, 35(9):1–5, May 2008. ISSN 0094-8276. doi: 10.1029/2008GL033256. URL http://www.agu.org/pubs/crossref/2008/2008GL033256.shtml.